40-Gb/s Widely Tunable Low-Drive-Voltage Electroabsorption-Modulated Transmitters

James W. Raring, *Member, IEEE,* Leif A. Johansson, *Member, IEEE,* Erik J. Skogen, *Member, IEEE,* Matthew N. Sysak, *Member, IEEE,* Henrik N. Poulsen, Steven P. DenBaars, *Fellow, IEEE,* and Larry A. Coldren, *Fellow, IEEE*

Invited Paper

***Abstract*—We present the first 40-Gb/s widely tunable electroabsorption modulator (EAM)-based transmitters. The sampled-grating Distributed Bragg Reflector (SG-DBR) laser/EAM devices were fabricated using a multiple-band-edge-quantum-well-intermixing (QWI) technique, which requires only simple blanket regrowth and avoids disruption of the axial waveguide. Devices were fabricated from two different multiple quantum well (MQW) active-region designs for direct comparison. The SG-DBR lasers demonstrated 30 nm of tuning with output powers up to 35 mW. The integrated QW EAMs provided 3-dB optical modulation bandwidths in the 35–39 GHz range, low-drive voltage (1.0–1.5 V_{PtoP}), and low/negative-chirp operation. Bit-error-rate measurements at 40 Gb/s demonstrated 0.2–1.1 dB of power penalty for transmission through 2.3 km of standard fiber.**

***Index Terms*—Chirp, electroabsorption modulators (EAMs), laser tuning, optical-fiber communication, quantum-well-intermixing (QWI), semiconductor lasers, wavelength-division multiplexing (WDM).**

I. Introduction

Electroabsorption-modulated lasers are candidate sources for 40-Gb/s very-short-reach (VSR) router-to-router interconnect applications, as they are compact, potentially low-cost, and can facilitate low-drive voltages with high-modulation bandwidth [1]. The monolithic integration of electroabsorption modulators (EAMs) with widely tunable lasers allows for inventory reduction and wavelength agile functionality in communication systems based on wavelength-division multiplexing (WDM). An EAM making use of a quantum-well (QW) absorber region exploits the quantum-confined Stark effect offering increased efficiency over bulk Franz–Kelydsh-type EAMs [2]. Additionally, QW-EAMs can enable negative-chirp operation for efficient transmission at high bit-rates, where fiber dispersion is increasingly important.

We present the first QW-EAM-based 40-Gb/s widely tunable transmitter devices. Previous reports of 40-Gb/s QW-EAMs either did not include an integrated laser or included a single-frequency distributed-feedback laser [1], [3], [4]. In this paper, we demonstrate widely tunable transmitters fabricated using a simple and robust quantum-well-intermixing (QWI) processing platform to avoid the traditional fabrication complexity necessary for the integration of negative-chirp EAMs with diode lasers.

The conventional method for the realization of a single-chip-diode laser/QW-EAM transmitter involves the selective removal of the as-grown multiple quantum well (MQW) for use in laser gain regions followed by the regrowth of an MQW with a higher band edge for use in the EAMs. This method is commonly referred to as butt-joint regrowth [1], [5]. Although the butt-joint regrowth process does facilitate high flexibility, it requires etching and defining a regrowth interface in the core of the optical waveguide. The difficulty associated with matching the thickness and achieving the desired composition to avoid reflection and loss at the interface is great [5]. Another technique used to realize multiple band edges across a wafer is selective-area growth. However, the abruptness of the transition region is limited by the surface diffusion of the growth constituents, which may be on the order of tens of micrometers. Additionally, the optical mode overlap with the MQW may not be ideal in all sections due to the thickness variation. The relatively simple QWI process employed in this work enables the precise placement of the band edge of each component within the device, allowing for blue-shifted QWs to remain in the modulator while leaving the axial waveguide undisturbed.

The widely tunable transmitters presented in this paper consists of an EAM with partially intermixed QWs and a sampled-grating DBR (SG-DBR) laser with as-grown QWs in the gain region and severely intermixed QWs in the passive and tuning sections. We explore two different centered-multiple QW (c-MQW) active-region designs. The first design uses ten 6.5-nm wells to yield a confinement factor of 12.6% while the second design makes used of fifteen 8.0-nm wells to yield a confinement factor of 25.0%. The increased number of wells in the 15 MQW is expected to result in improved EAM efficiency at the expense of somewhat degraded laser performance.

The 10- and 15-MQW transmitters exhibit 30 nm of tuning with high output power. The 10-MQW EAMs demonstrated

Manuscript received June 14, 2006; revised September 28, 2006.

J. W. Raring, L. A. Johansson, E. J. Skogen, M. N. Sysak, H. N. Poulsen, and L. A. Coldren are with the Electrical and Computer Engineering Department, University of California, Santa Barbara, CA 93106-2030 USA (e-mail: jraring@engineering.ucsb.edu; leif@ece.ucsb.edu; skogen@engineering.ucsb.edu; mnsysak@engineering.ucsb.edu; henrik@ece.ucsb.edu; coldren@ece.ucsb.edu).

S. P. DenBaars is with the Materials Department, University of California, Santa Barbara, CA 93106-2030 USA (e-mail: denbaars@engineering.ucsb.edu).

Digital Object Identifier 10.1109/JLT.2006.886722

0733-8724/$25.00 © 2007 IEEE

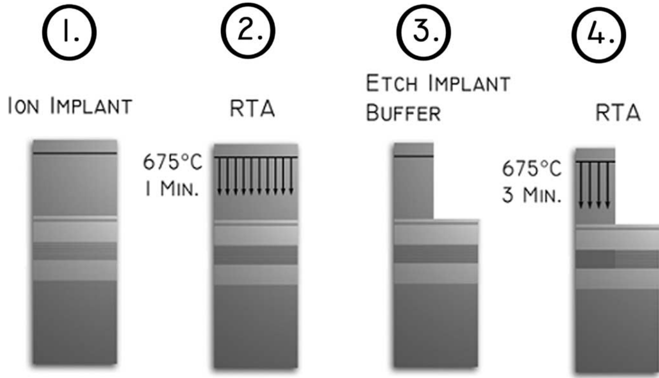

Fig. 1. Step-by-step schematic of the intermixing process. From left to right: ion implantation; RTA; buffer-layer removal; and further annealing.

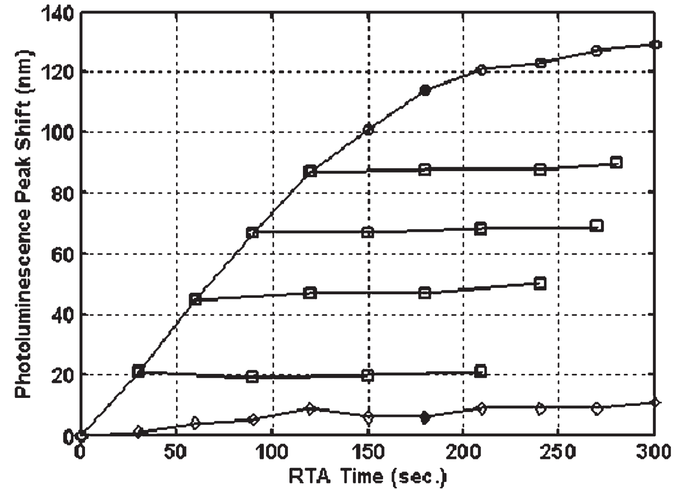

Fig. 2. PL peak shift as a function of anneal time, showing the initial linear increase in the peak shift and the complete halting of the peak shift for samples for which the implant buffer layer has been etched. Symbols indicate nonimplanted (triangles), implanted (circles), and samples with partial anneal followed by the removal of the implant buffer layer (squares).

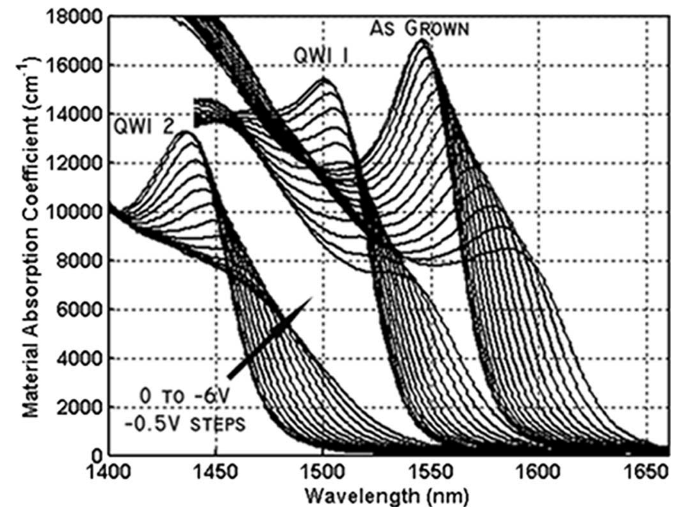

Fig. 3. Material-absorption coefficient versus wavelength for photodiodes fabricated from as-grown material and material intermixed to two different levels.

3-dB optical modulation bandwidths of up to 39 GHz, 1.5-V_{PtoP} drive voltages, power penalties of 0.2–0.5 dB for 40-Gb/s transmission through 2.3 km of fiber across the tuning range of the laser. The 15-MQW EAMs demonstrated 3-dB optical modulation bandwidths of up to 35 GHz, 1.0-V_{PtoP} drive voltages, power penalties of 0.7–1.1 dB for 40-Gb/s transmission through 2.3 km of fiber across the tuning range of the laser.

II. BACKGROUND

A. QWI Integration Platform

QW intermixing allows for the strategic postgrowth tuning of the QW band edge using a relatively simple procedure. Since this technique enables the employment of c-MQW active regions for maximized modal gain lasers and blue-shifted QWs for use in EAMs, QWI breaks the complexity tradeoff associated with the flexible butt-joint regrowth and SAG integration schemes. QWI makes use of the metastable nature of the compositional gradient found at heterointerfaces. The natural tendency for materials to interdiffuse is the basis for the intermixing process. Since QWI does not change the average composition but only slightly changes the compositional profile, there is a negligible index discontinuity at the interface between adjacent sections. This eliminates parasitic reflections that can degrade performance.

In this paper, we employ the implant-enhanced interdiffusion QWI technique illustrated in the step-by-step diagram of Fig. 1. This method has been shown to have good spatial resolution and is controllable using anneal time, temperature, and implant dose [6]. Furthermore, we can achieve any number of QW band edges in the structure using selective removal of the catalyst. In the first step of Fig. 1, a selective P^{+} implantation is performed to introduce point defects in an unintentionally doped sacrificial InP implant buffer layer grown above the MQW active region. Next, a rapid-thermal-anneal (RTA) step is performed to shift the MQW band edge to that desired in the EAM regions. Once the EAM band edge is reached, the point defects are removed in the EAM region by selective removal of the InP implant buffer layer. The anneal is then continued until the desired band edge is reached for the passive and tuning sections. Once all the desired band edges have been defined, the remaining buffer layer is removed and the p-cladding regrowth is performed. The buffer-layer etch and RTA sequence can be repeated to achieve any number of band edges across the wafer. This capability is demonstrated in Fig. 2 with a plot of photoluminescence (PL) peak versus anneal time for samples with and without implantation and samples with the implant buffer layer removed at intermediate anneal steps.

To realize an optimized QW-EAM, it is crucial that the QWI process does not significantly degrade the absorption characteristics of the as-grown MQW. This effect was studied using photocurrent spectroscopy on photodiodes fabricated with as-grown material ($\lambda_{PL} = 1545$ nm) and material intermixed to two different levels, QWI 1 ($\lambda_{PL} = 1500$ nm) and QWI 2 ($\lambda_{PL} = 1430$ nm). The absorption coefficient contours versus wavelength for photodiodes biased from 0 to -6 V in -0.5-V increments are shown in Fig. 3. The photodiode

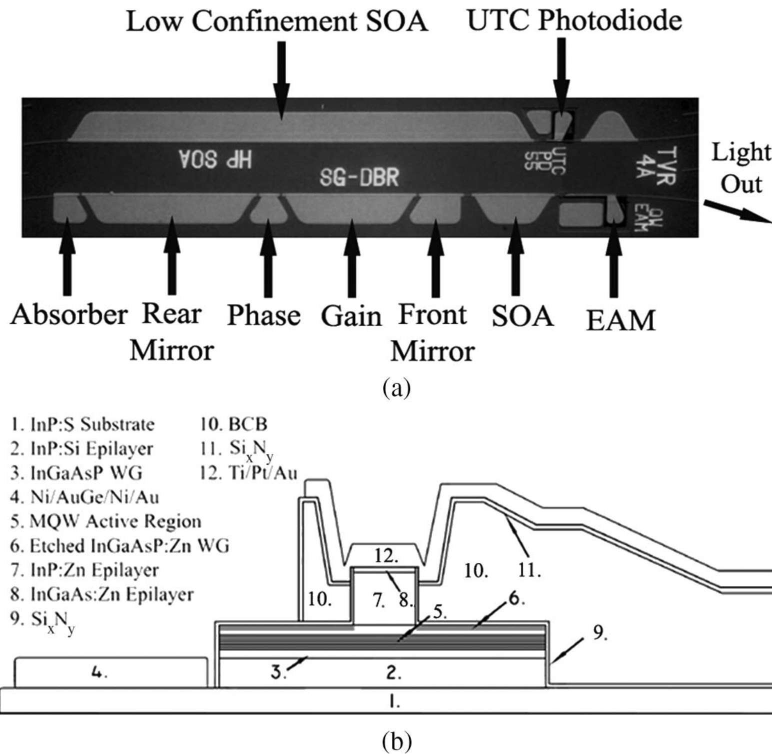

Fig. 4. (a) Top-view SEM of the device architecture, where the SG-DBR/EAM transmitter device is positioned on the lower ridge. (b) Cross-sectional schematic of modulator sections.

devices contained seven 6.5-nm compressively strained QWs and eight 8.0-nm barriers sandwiched between two 120-nm waveguide layers. As expected, the exciton peak shifts to shorter wavelengths as the degree of intermixing is increased and the quantized energy levels are separated. The exciton strength is somewhat decreased with intermixing due to the wider/shallower nature of the intermixed well, which reduces the exciton confinement. However, the exciton remains as a dominant characteristic in the absorption spectra, especially in the material shifted by only ∼45 nm (QWI 1), which represents a band-edge detuning in the vicinity required for optimal EAM performance.

B. Device Architecture

The transmitters reported here were part of integrated-transceiver devices. A top-view scanning-electron-micrograph (SEM) image of the parallel-surface-ridge waveguide architecture is shown in Fig. 4(a). The optical receiver [upper ridge in Fig. 4(a)] consists of a low-confinement factor semiconductor optical amplifier (SOA) followed by a unitraveling-carrier (UTC) photodiode. In this paper, we focus on the optical transmitter [lower ridge in Fig. 4(a)] consisting of a five-section SG-DBR laser followed by a 250-μm-long output SOA and a 125-μm-long EAM. The five sections of the SG-DBR laser are, from left to right in Fig. 4(a): backside absorber; rear mirror; phase; gain; and front mirror. The output waveguide is simultaneously flared from 3 to 5.5 μm in width and curved to reach a final facet angle of 6.5° to minimize reflections.

C. SG-DBR Laser

The SG-DBR mirror is a special form of the DBR mirror, where the gratings are periodically blanked in order to create a comblike reflectivity spectrum [7]. The lithographically defined SG mirrors make this laser ideal for monolithic integration. By differing the sampling periods in the front and back mirrors, the peak reflectivity spacing of the mirrors will differ so that only one set of reflectivity peaks is aligned within the desired tuning range. By differentially tuning the front and back mirrors, a small amount adjacent reflectivity peaks can be aligned and the laser will operate at this new widely spaced wavelength. The simultaneous tuning of front and back mirrors allows wavelength coverage between mirror reflectivity peaks. The phase section provides cavity-mode tuning, which ensures that the laser cavity mode is aligned with the mirror reflectivity peaks. The tuning in the mirrors and phase sections is based on carrier injection, producing a negative change in refractive index.

D. EAM

In an EAM, a reverse bias is used to shift the band edge of the modulator section to a lower energy, thereby increasing the absorption of that region. In our case, QWI only smears the interfaces between the QWs and barriers, such that the QWs still remain intact after the intermixing, although slightly shallower and rounded. To achieve high-speed operation, we minimize the capacitance associated with the EAM. The low-k dielectric benzocyclobutene (BCB) is defined underneath the p-electrode, a short dry etch is performed adjacent to the ridge to eliminate a thin diffused Zn layer, and the diode length and

p-electrode area are minimized. A cross-sectional schematic of the EAM is shown in Fig. 4(b).

III. Process

Two different epitaxial-base-structure MQW designs were explored in this paper. The first consisted of 10 InGaAsP 6.5-nm compressively strained (0.9%) QWs and 11 8.0-nm tensile-strained (0.3%) InGaAsP barriers yielding a conduction-band offset of 115 meV. The 10 MQW was centered within two 105-nm 1.3Q waveguide layers designed for maximum modal confinement (12.6%). The second MQW design consisted of 15 InGaAsP 8.0-nm compressively strained (0.6%) QWs and 16 8.0-nm tensile-strained (0.3%) InGaAsP barriers yielding a conduction-band offset of 85 meV. The lower band offset of the 15-MQW design was intended to promote the uniform filling of carriers in the wells under forward bias. The 15 wells were centered within two 60-nm 1.3Q waveguide layers designed for maximum modal confinement (25.0%). The metal-organic chemical-vapor-deposition grown epitaxial base structures initiated on a conducting InP substrate. The growth sequence began with 1.8 μm of InP:Si, followed by the c-MQW active region, a 25-nm InP regrowth layer, a 20-nm 1.3Q stop etch, and a 450-nm InP implant buffer layer.

A 500-nm $\mathrm{Si}_x\mathrm{N}_y$ mask layer was deposited using plasma-enhanced chemical vapor deposition and lithographically patterned such that it remained only over the active regions of the samples. Next, ion implantation was performed using P^+ at an energy of 100 keV, with a dose of 5E14 cm^{-2}, yielding a damage range of 90 nm, at a substrate temperature of 200 °C. The point defects created during the P^+ implant were then partially diffused through the structure using a 675-°C RTA step to shift the as-grown MQW band edge ($\lambda_{\mathrm{PL}} = 1540$ nm) to the desired EAM band edge ($\lambda_{\mathrm{PL}} = 1505$ nm). The implant buffer layer above the EAM sections was removed using a wet-etching process designed to terminate on the 1.3Q stop-etch layer. The samples were then subjected to an additional RTA step to severely blue-shift the passive and tuning sections, where the implant buffer layer remained. The resulting peak PL wavelength of these passive sections was 1440 nm in the 10-MQW sample and 1460 nm in the 15-MQW sample. Upon completion of the QWI process, the PL spectra of the three different bandgap regions was characterized from the actual 10-MQW and 15-MQW device samples. As shown in Fig. 5(a) and (b), the as-grown and EAM PL peaks are nearly identical in the 10- and 15-MQW devices.

Following the QWI process, two blanket regrowth and etch sequences were performed for the definition of the low-confinement SOA and UTC photodiode-receiver structures. Details of these structures can be found elsewhere [8], [9]. Finally, the InP:Zn cladding and the InGaAs:Zn contact layers were grown. Standard lithography and etch techniques were carried out for the definition 3-μm-wide surface-ridge devices. The wafers were thinned; the devices were cleaved into bars and antireflection coated. The die were separated, soldered to aluminum-nitride carriers, and wire bonded for characterization. A scanning electron micrograph (SEM) image of the completed devices mounted on a carrier is shown in Fig. 6.

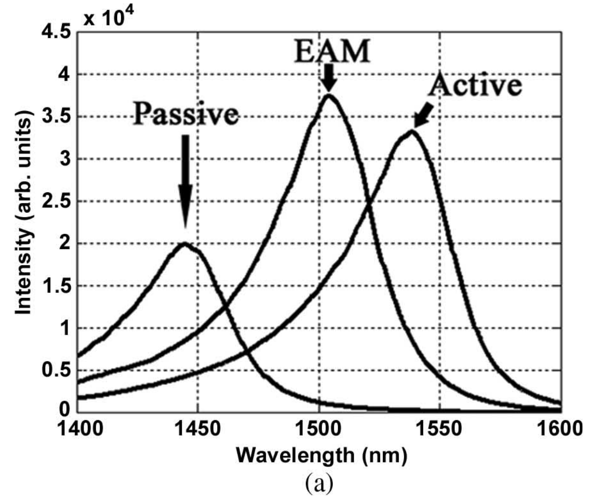

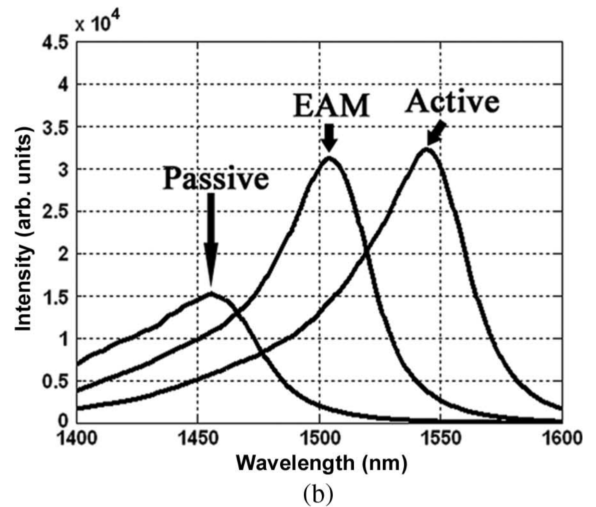

Fig. 5. PL spectra of active, EAM, and passive sections rendered using QWI for the (a) 10-MQW and (b) 15-MQW devices. Data taken from actual device chips previous to regrowth steps.

Fig. 6. SEM image of transmitter device mounted on a carrier.

IV. Device Results

To extract the laser parameters and determine the material/processing quality, 3-μm-wide Fabry–Pérot (FP) active and active/passive ridge lasers were fabricated on the same chip as the transmitters and subjected to pulsed testing. The inverse

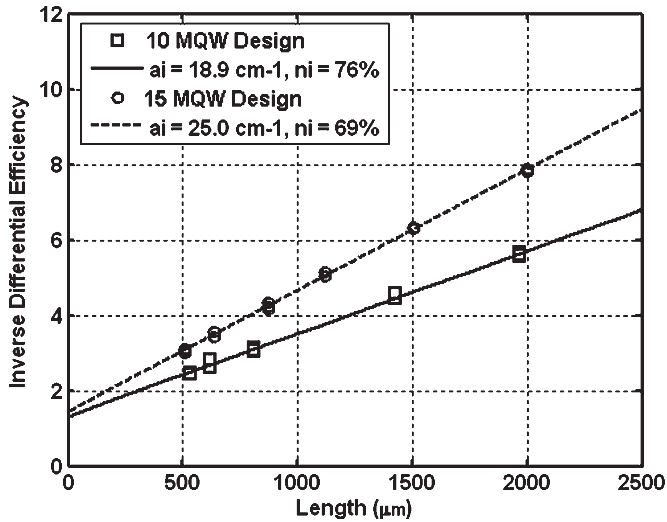

Fig. 7. Plot of inverse differential efficiency versus active FP laser length for lasers fabricated from 10- and 15-MQW base structures.

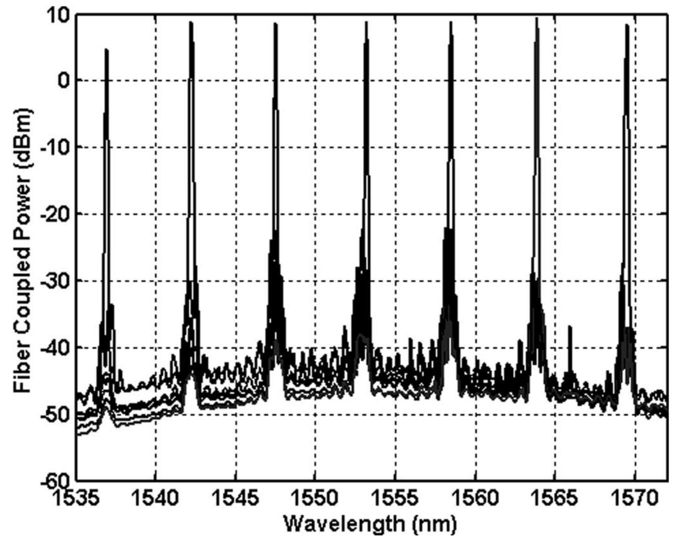

Fig. 8. Superimposed output spectrums tuned to different lasing wavelengths for SG-DBR lasers fabricated from 10-MQW base structure.

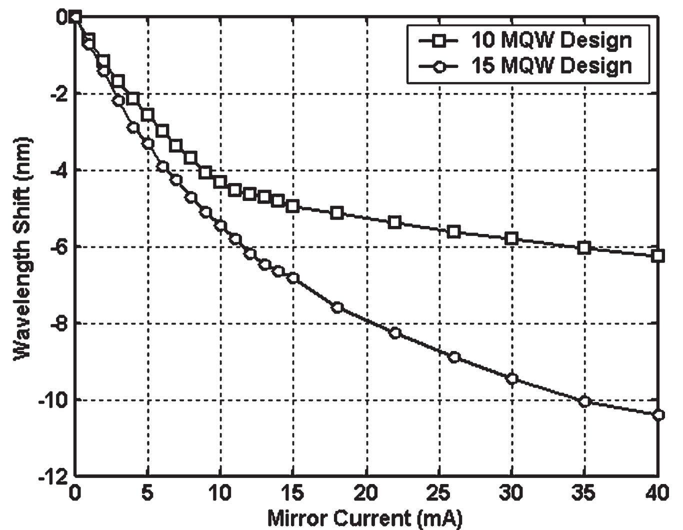

Fig. 9. Wavelength shift versus applied current to front mirror in SG-DBR laser fabricated from 10-MQW and 15-MQW base-structure designs.

differential efficiency is plotted versus active FP laser length in Fig. 7. As shown in the figure, the 10-MQW device demonstrated an injection efficiency (ni) of 76% with a modal loss (ai) of 18.9 cm^{-1} while the 15-MQW device demonstrated an injection efficiency of 69% with a modal loss of 25.0 cm^{-1}. The higher confinement factor of the 15 MQW will lead to an increased modal loss and the greater number of wells will likely reduce the injection efficiency. However, the higher confinement factor of the 15-MQW device will increase the modal gain and somewhat compensate the degraded loss and injection efficiency.

The cleave-back method described in [10] was used to characterize the passive and EAM loss in both MQW designs at a wavelength of 1550 nm. The passive loss was extracted to be 1.8 cm^{-1} and the EAM loss was found to be 13 cm^{-1} in the 10-MQW design. This corresponds to a passive propagation loss of under 1 dB/mm and an unbiased insertion loss of under 1 dB for a 125-μm-long EAM at 1550 nm. The passive propagation loss can largely be attributed to the free-carrier absorption in the p-cladding and waveguide scattering. However, the stated loss value is very acceptable in these devices as the total passive waveguide length is less than 0.5 mm. In the 15-MQW design, the passive loss was extracted to be 4.0 cm^{-1} and the EAM loss was found to be 24.5 cm^{-1}. This corresponds to a passive propagation loss of under 2 dB/mm and an unbiased insertion loss of under 1.5 dB for a 125-μm-long EAM. The increased losses associated with the 15-MQW design is likely caused by the increased band-tail absorption, which results from the $\sim 2\times$ higher confinement within the wells and the slightly lower band-gap energy in the passive sections.

The continuous wave performance of the transmitters was characterized at a stage temperature of 18 °C. The surface-ridge SG-DBR lasers fabricated from the 10-MQW and 15-MQW active-region designs both demonstrated over 30 nm of continuous tuning from wavelengths of 1536–1569 nm. Superimposed output spectrums for lasing wavelengths across the SG-DBR tuning band are shown in Fig. 8 for a 10-MQW device with the laser-gain section and a 250-μm-long output SOA biased at 100 mA. The laser/SOA output light passed through the unbiased EAM and curved/flared waveguide before being coupled into a conical-tipped lensed fiber, with an estimated coupling loss of 4.5 dB. As shown in Fig. 8, the device demonstrated fiber-coupled output powers of up to 10 dBm with a side-mode suppression ratio of over 35 dB for wavelengths from 1542 to 1569 nm. By design, a wavelength shift of over 5.4 nm must be achieved through current injection to tune between the adjacent reflectivity peaks for continuous tuning across the entire supermode spectrum. To characterize the tuning efficiency of both active-region types, the wavelength shift was characterized as a function of current injected into the front mirror. As shown in Fig. 9, both MQW designs easily provide the required 5.4 nm of shift for continuous tuning. However, the 15-MQW design facilitates increased efficiency requiring only $\sim$10 mA to achieve such a value while the 10-MQW design requires $\sim$20 mA for an equivalent shift. The increased tuning efficiency of the 15-MQW device can be explained by the $\sim 2\times$ greater modal

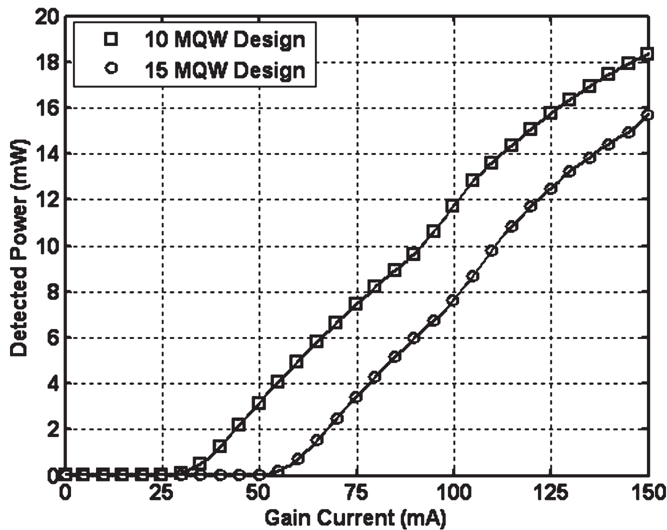

Fig. 10. On-chip laser output power versus gain current for SG-DBR lasers fabricated from the 10-MQW and 15-MQW base-structures designs.

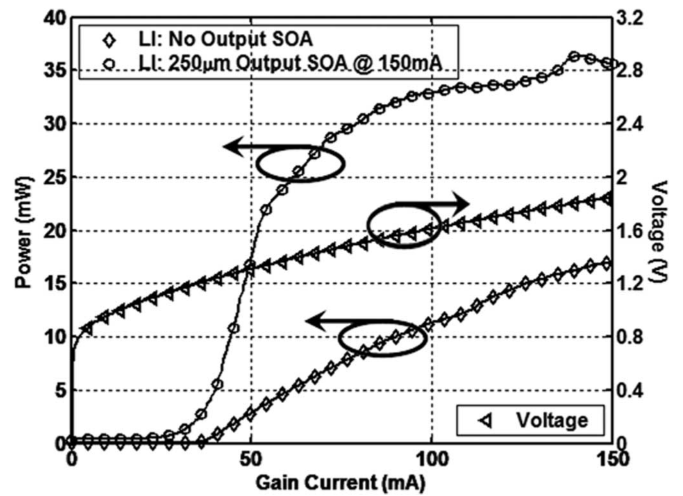

Fig. 11. Output power of 10-MQW SG-DBR laser captured in an integrating sphere for the case with no output SOA and with a 250-μm-long SOA. The voltage is depicted on the right-hand y-axis.

overlap with the lower bandgap QW material than that of the 10-MQW device [11].

By reverse biasing the SOA placed directly after the front mirror of the SG-DBR laser, the on-chip light out versus applied gain current can be measured. This is an excellent means to evaluate the SG-DBR laser performance without the influence of the EAM insertion loss, passive propagation loss, or fiber-coupling loss, since the SOA is positioned immediately following the laser in a continuous waveguide. In Fig. 10, the on-chip light versus current is plotted for SG-DBR lasers fabricated from the 10- and 15-MQW base structures. The 10-MQW device demonstrated a threshold current of ~30 mA while the 15-MQW SG-DBR laser required ~55 mA to reach threshold. The increased threshold current in the 15-MQW device scales closely with the increase in active-region volume over the 10-MQW device indicating that nonuniform pumping of the 15 wells is not significantly degrading the device performance.

The on-chip light versus current measurement does not account for the EAM insertion loss or passive waveguide loss that occurs before the light exits the chip and becomes useful to the external world. To determine the net device output power, the light is detected in an integrating sphere. In this configuration, the light exits the laser or laser/SOA and is then passed through the unbiased EAM, curved/flared output waveguide, and captured into an integrating sphere. Fig. 11 plots the output power and voltage versus gain current (LIV) for SG-DBR lasers fabricated from the 10-MQW active-region design for a device with no output SOA and for a laser with a 250-μm-long SOA positioned after the front mirror. At a gain current of 150 mA, the 10-MQW device demonstrates over 16 mW of output power with no output SOA and over 35 mW of output power with an output SOA biased at 150 mA. At the same gain current, the 15-MQW device produces 12 mW with no output SOA and over 18 mW with an output SOA biased at 150 mA. The lower output power of the 15-MQW device with no SOA is a result of higher modal loss, reduced injection efficiency, and the increased threshold current coupled with the increased passive waveguide loss and EAM insertion loss. The ~2× greater confinement factor of the 15-MQW active-region design results in a reduced SOA saturation power, and hence, further limits the output power of the 15-MQW SG-DBR/SOA device. Thus, the 10-MQW device employing an output SOA demonstrates a significantly higher output power than the 15-MQW device.

The dc extinction from 125-μm-long EAMs in both the 10- and 15-MQW transmitters are shown in Fig. 12(a) and (b), respectively. The 10-MQW device provides 20–30 dB of total extinction with slope efficiencies of 14–16 dB/V for wavelengths from 1536 to 1560 nm. The 15-MQW device provides 25–33 dB of total extinction with slope efficiencies of 19–23 dB/V for wavelengths from 1542 to 1565 nm. The efficient EAM extinction properties are due to the combination of the high confinement factors associated with the c-MQW designs and the intermixing process that allows for precise placement of the modulator band edge.

The small signal-frequency response of the EAMs was measured using a 50-GHz network analyzer. The EAM electrodes were directly probed using ground-signal probes with a 50-Ω termination load. The stage temperature was again maintained at 18 °C. The electrical to optical response of the 10- and 15-MQW 125-μm-long modulators is shown in Fig. 13. The optical 3-dB modulation bandwidth was measured to be 39 GHz in the 10-MQW EAM and 35 GHz in the 15-MQW EAM. The slightly higher modulation bandwidth of the 10-MQW device is a result of a thicker BCB layer used underneath the p-electrode.

The large signal chirp was measured for both device types at 10 Gb/s for wavelengths from 1541 to 1564 nm using Agilent's Time Resolved Chirp software. The chirp parameter was measured as a function of the dc bias applied to the EAM with a 1.5-V_{PtoP} drive applied to the 10-MQW device and 1.0-V_{PtoP} drive applied to the 15-MQW device. As shown in Fig. 14, the chirp parameter is reduced with increasing reverse bias and decreasing wavelength. The measurement demonstrates negative-chirp values for the 15-MQW device at reverse-bias levels ranging from 1.5 to 2.8 V. An issue with the test set limited the measurement range in the 10-MQW device such

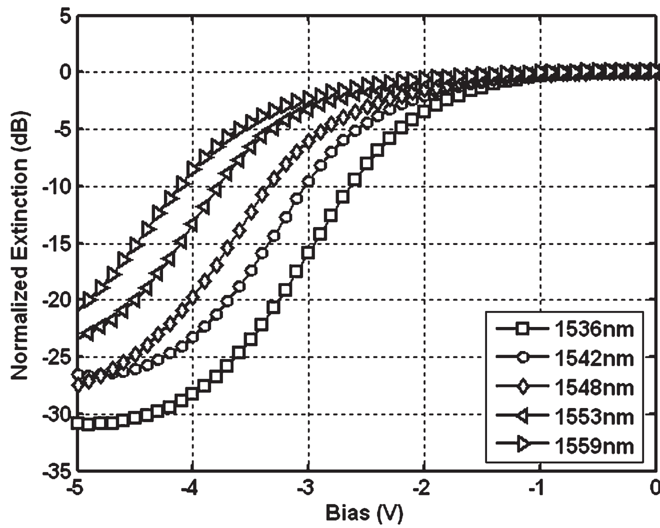

(a)

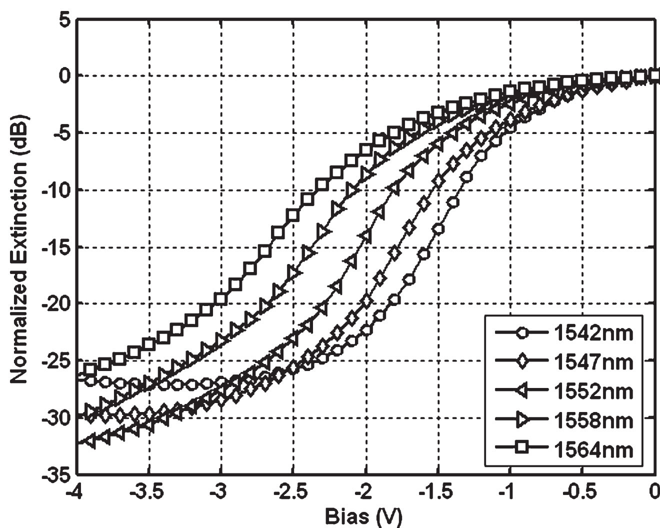

(b)

Fig. 12. Broadband dc extinction of a 125-μm modulator fabricated from the (a) 10-MQW base-structure and (b) 15-MQW base-structure design.

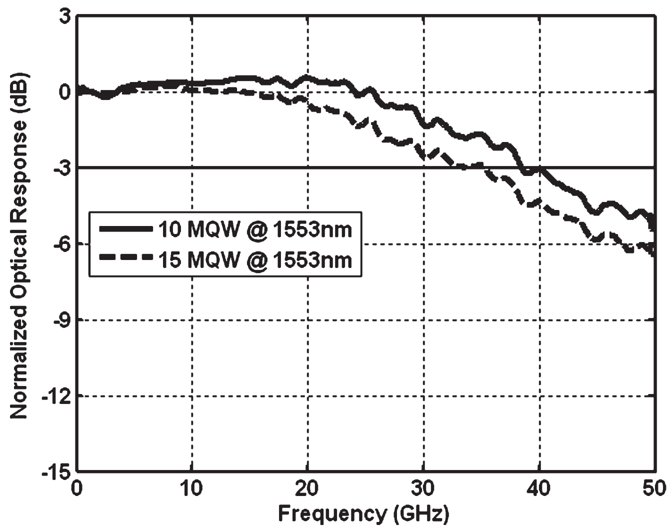

Fig. 13. Electrical-to-optical small signal response of 125-μm EAMs using 10- and 15-MQW designs.

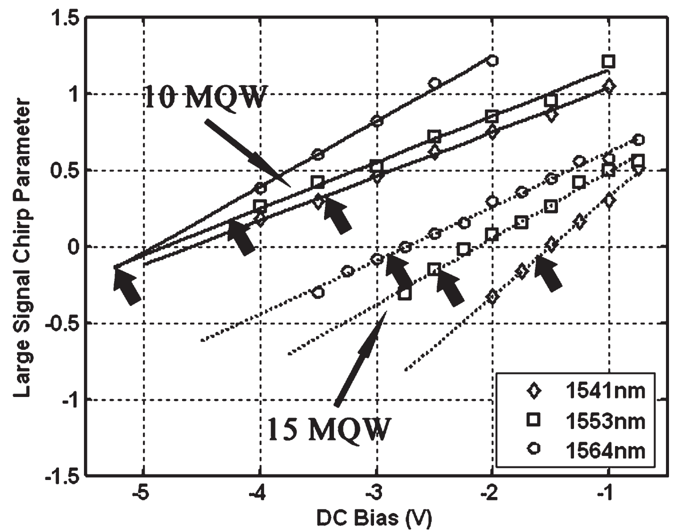

Fig. 14. Broadband large signal chirp parameter of EAMs using the 10-MQW ($1.5\ \mathrm{V_{PtoP}}$) and 15-MQW ($1.0\ \mathrm{V_{PtoP}}$) designs with arrows indicating dc bias used for 40-Gb/s eye diagrams shown in Fig. 15.

that the lowest measured chirp value was 0.15. However, the chirp parameter approaches negative values in the reverse bias range of 4.5–5.0 V. The lower required bias for negative chirp in the 15-MQW design is a result of the wider/shallower wells allowing for a greater Stark shift. The increased required reverse bias with increasing wavelength correlates with that reported in [12] and is perfectly reasonable when considering the proximity of the modulator band edge to the laser-operating wavelength. While the general shape of the absorption curves remain the same, the onset of absorption with reverse voltage increases and the absorption efficiency decreases somewhat with increasing wavelength.

Nonreturn-to-zero eye diagrams were taken at 40 Gb/s with a pseudorandom bit sequence (PRBS) of $2^{31}-1$ over the tuning range of the SG-DBR lasers for both MQW designs. In Fig. 15(a), the back-to-back input eye along with device output eyes are shown for the 10-MQW EAM with a 1.5-$\mathrm{V_{PtoP}}$ drive. As depicted in the figure, extinction ratios (ER) greater than 8.7 dB are demonstrated for wavelengths up to 1560 nm with dc-bias levels ranging from 3.4 to 5.2 V. The average fiber-coupled output power of this device ranged from -5 to 0 dBm. In Fig. 15(b), the back-to-back input eye along with device output eyes are shown for the 15-MQW EAM. Due to the increased efficiency offered by the 15-MQW device, a 1.0-$\mathrm{V_{PtoP}}$ drive was used. As depicted in the figure, the ERs ranged from 6.8 to 7.8 dB for wavelengths from 1542 to 1559 nm with dc-bias levels ranging from 1.6 to 2.6 V. The average fiber-coupled output power of this device ranged from -10 to -5 dBm. The dc bias points for the eye diagrams from both the 10- and 15-MQW EAMs in Fig. 15 are indicated with arrows in Fig. 14 to demonstrate the expected chirp at these operating points. As shown, the predicted chirp for the 10-MQW EAMs range from -0.1 to 0.3, and for the 15 MQW, the chirp parameter is negative in all cases. The discrepancy between the RF ERs shown in Fig. 15 and the dc-extinction-efficiency data of Fig. 12 predicting 14–16 dB/V for the 10-MQW device and 19–23 dB/V for the 15-MQW device indicates the presence of RF losses.

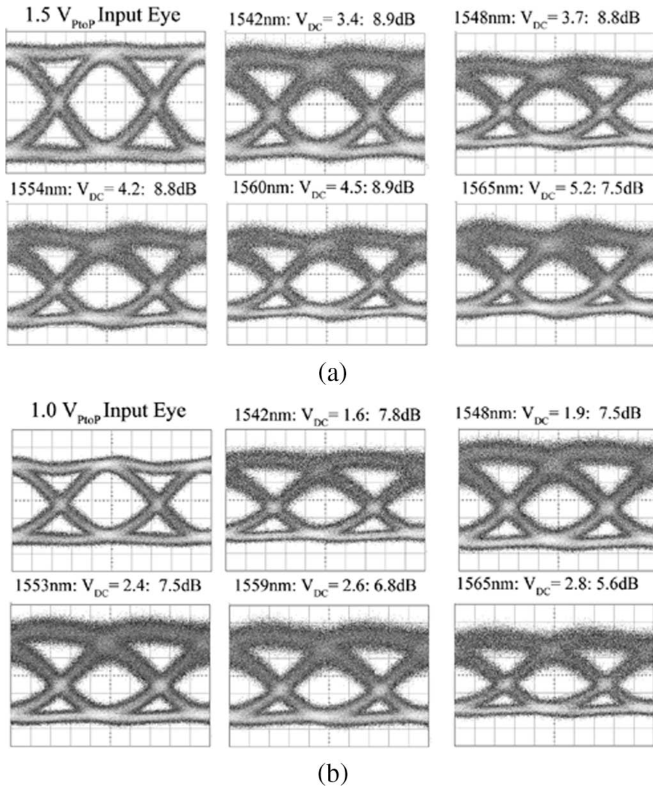

Fig. 15. 40-Gb/s eye diagrams from the (a) 10-MQW device with a 1.5-V_{PtoP} drive and (b) the 15-MQW device with a 1.0-V_{PtoP} drive.

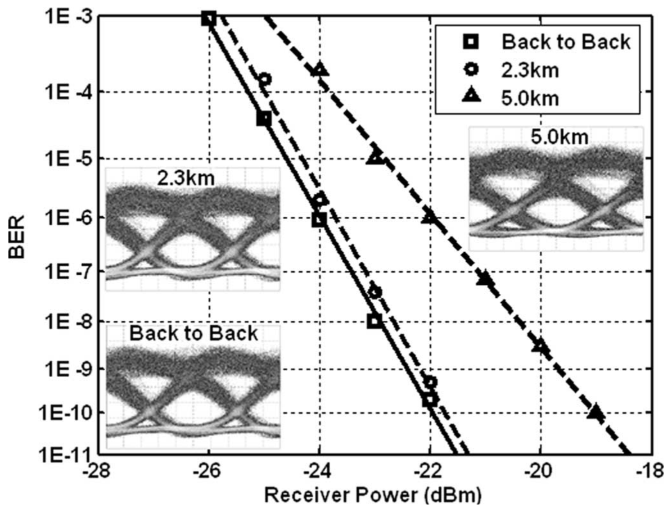

Fig. 16. BER measurements from 10-MQW device at 40 Gb/s with a 1.5-V_{PtoP} drive and a wavelength of 1553 nm. The back-to-back eye diagram along with the eye diagrams after transmission shown as insets.

This is most likely a result of the impedance mismatch between the source and device causing significant electrical reflections. This problem could be corrected with an impedance-matched-electrode design to yield improved RF efficiency.

Bit-error-rate (BER) measurements were made for 40-Gb/s transmission through 2.3 and 5 km of standard Corning SMF-28 fiber. A PRBS of $2^7 - 1$ was used due to a noise floor in the BER test setup that manifested itself at longer word lengths. In Fig. 16, the BER results and the respective eye diagrams are shown for the 10-MQW device at a wavelength of 1553 nm using a 1.5-V_{PtoP} drive and a dc bias of 4.9 V. As shown in the figure, the transmitter demonstrated only 0.2 dB of power penalty through 2.3 km and 2.3 dB of penalty through 5.0 km at a BER of 1E-9. Fig. 17 plots the 40-Gb/s power penalty at a BER of 1E-9 for transmission through 2.3 km of fiber across the tuning band of both the 10- and 15-MQW transmitters. The dc operating points are depicted in the figure. The 10-MQW device demonstrates between 0.2 and 0.5 dB of power penalty for transmission through 2.3 km of fiber at wavelengths spanning from 1543 to 1565 nm, while the 15-MQW device demonstrates between 0.7 and 1.1 dB of penalty. According to Fig. 14, the dc operating points are expected to provide slightly negative chirp.

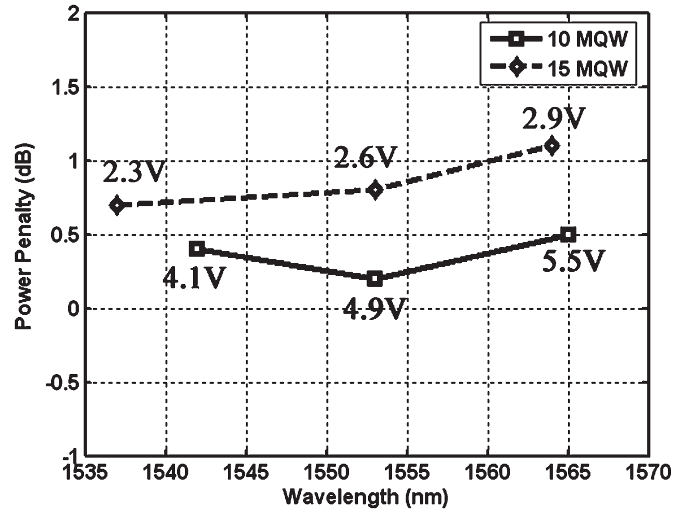

Fig. 17. Broadband 1E-9 BER power penalty for 40-Gb/s transmission through 2.3 km of fiber for both the standard 10-MQW base structure and the modified 15-MQW base-structure design.

V. Conclusion

We have demonstrated the first widely tunable EAM-based transmitters operating at 40 Gb/s. This paper was made possible by a robust QWI technique for the precise placement of multiple band edges to achieve high-modulation efficiency from relatively short EAMs. Two different active-region designs were explored. The 10-MQW SG-DBR lasers demonstrated threshold currents of ~30 mA, output powers up to 35 mW, and over 30 nm of tuning. The 15-MQW SG-DBR laser demonstrated threshold currents of ~55 mA, output powers up to 18 mW, and over 30 nm of tuning. The 3-dB optical modulation bandwidth of the 125-μm-long EAMs was 39 and 35 GHz for the 10- and 15-MQW devices, respectively. Although the additional wells of the 15-MQW design slightly degraded the laser performance, the dc extinction efficiency was increased from 16 dB/V in the 10-MQW EAM to 23 dB/V in the 15-MQW EAM. This allowed for slightly lower drive voltage at 40 Gb/s with the 10-MQW EAM requiring 1.5 V to achieve a ~9-dB ER and 1.0 V for the 15-MQW EAM to achieve an ~8-dB ER. Both EAMs demonstrated low- to negative-chirp operation. Fiber-transmission experiments demonstrated low-power penalties of 0.2–1.1 dB for 40-Gb/s transmission through 2.3 km of fiber across the tuning range of the lasers.

References

[1] M. Okayasu *et al.*, "A 1550-nm 40-Gb/s electro-absorption DFB laser diode module for transponders with very short reach ($<$ 2 km) applications," in *LEOS Tech. Dig.*, 2004, pp. 513–514, Paper WG2.

[2] M. K. Chin, "Comparative analysis of the performance limits of Franz–Keldysh effect and quantum confined Stark effect electroabsorption waveguide modulators," *Proc. Inst. Electr. Eng.—Optoelectron.*, vol. 142, no. 2, pp. 109–114, Apr. 1995.

[3] H. Fukano, T. Yamanaka, M. Tamura, Y. Kondo, and T. Saitoh, "Very low driving voltage InGaAlAs/InAlAs electroabsorption modulators operating at 40 Gb/s," *Electron. Lett.*, vol. 41, no. 4, pp. 211–212, Feb. 2005.

[4] P. Gerlach *et al.*, "40-Gb/s operation of laser-integrated electroabsorption modulator using identical InGaAlAs quantum," in *Proc. Int. Conf. Indium Phosphide and Rel. Mater. Tech. Dig.*, 2005, pp. 554–557.

[5] J. Binsma, P. Thijs, T. VanDongen, E. Jansen, A. Staring, G. VanDenHoven, and L. Tiemeijer, "Characterization of butt-joint InGaAsP waveguides and their application to 1310 nm DBR-type MQW Ganin-Clamped semiconductor optical amplifiers," *IEICE Trans. Electron.*, vol. E80-C, no. 5, pp. 675–681, May 1997.

[6] S. Charbonneau, E. Kotels, P. Poole, J. He, G. Aers, J. Haysom, M. Buchanan, Y. Feng, A. Delage, F. Yang, M. Davies, R. Goldberg, P. Piva, and I. Mitchell, "Photonic integrated circuits fabricated using ion implantation," *IEEE J. Sel. Topics Quantum Electron.*, vol. 4, no. 4, pp. 772–793, Jul./Aug. 1998.

[7] V. Jayaraman, Z. Chuang, and L. Coldren, "Theory, design, and performance of extended tuning range semiconductor lasers with sampled gratings," *IEEE J. Quantum Electron.*, vol. 29, no. 6, pp. 1824–1834, Jun. 1993.

[8] J. Raring, E. Skogen, M. Mašanović, S. DenBaars, and L. Coldren, "Demonstration of high saturation power/high gain SOAs using quantum well intermixing and MOCVD regrowth," *Electron. Lett.*, vol. 41, no. 24, pp. 1345–1346, Nov. 2005.

[9] J. W. Raring, E. J. Skogen, C. S. Wang, J. S. Barton, G. B. Morrison, S. Demiguel, S. P. DenBaars, and L. A. Coldren, "Design and demonstration of novel quantum well intermixing scheme for the integration of UTC-Type photodiodes with QW-based components," *IEEE J. Quantum Electron.*, vol. 42, no. 2, pp. 171–181, Feb. 2005.

[10] E. Skogen, J. Barton, S. DenBaars, and L. Coldren, "A quantum-well-intermixing process for wavelength-agile photonic integrated circuits," *IEEE J. Sel. Topics Quantum Electron.*, vol. 8, no. 4, pp. 863–869, Jul./Aug. 2002.

[11] J. Shim, M. Yamaguchi, P. Delansay, and M. Kitamura, "Refractive index and loss changes produced by current injection in InGaAs(P)–InGaAsP multiple quantum-well (MQW) waveguides," *IEEE J. Sel. Topics Quantum Electron.*, vol. 1, no. 2, pp. 408–415, Jun. 1995.

[12] G. B. Morrison, J. W. Raring, E. J. Skogen, C. S. Wang, and L. A. Coldren, "Photocurrent spectroscopy analysis of widely tunable negative-chirp quantum well intermixed laser-modulator transmitters," *Appl. Phys. Lett.*, vol. 86, no. 7, pp. 1–3, Feb. 2005.

James W. Raring (M'06) was born in Ramsey, NJ, in 1978. He received the B.S. degree from the Materials Engineering Department, California Polytechnic State University, San Luis Obispo, in 2001 and the Ph.D. degree in materials science from the University of California, Santa Barbara, in 2006. His dissertation focuses on the design, growth, and fabrication of high-functionality wavelength-agile photonic integrated circuits operating at 10 and 40 Gb/s. The photonic circuits are based on sampled-grating DBR lasers, electroabsorption modulators, semiconductor optical amplifiers, and photodiodes.

He is currently with the Electrical and Computer Engineering Department, University of California, Santa Barbara. His work explores novel integration methods coupling quantum-well intermixing with straightforward metal–organic chemical-vapor-deposition regrowth steps. He has authored or coauthored more than 70 technical papers.

Dr. Raring is a member of IEEE Lasers and Electro-Optics Society, the Optical Society of America, and the International Society for Optical Engineers.

Leif A. Johansson (M'04) received the Ph.D. degree in engineering from University College London (UCL), London, U.K., in 2002.

He took up a postdoctoral position with the University of California, Santa Barbara, in 2002. His current research interests include design and characterization of integrated photonic devices for analog and digital applications.

Erik J. Skogen (M'04) was born in Minneapolis, MN, in 1975. He received the B.S. degree from Iowa State University, Ames, in 1997 and the M.S. and Ph.D. degrees from the University of California, Santa Barbara, in 1999 and 2003, respectively.

He is currently with the Electrical and Computer Engineering Department, University of California, Santa Barbara. His current research interests include widely tunable semiconductor lasers, monolithic integration for photonic integrated circuits, growth aspects in the InGaAsP material system using metal-organic chemical vapor deposition, and quantum-well intermixing.

Mathew N. Sysak (M'06) was born in Smithtown, NY, in 1976. He received the B.S. degree in chemical engineering from Pennsylvania State University, State College, in 1998.

He is currently with the Electrical and Computer Engineering Department, University of California, Santa Barbara. His current research interests include the monolithic integration of widely tunable semiconductor lasers with semiconductor optical amplifiers, electroabsorption modulators, and photodetectors in the InGaAsP material system.

Henrik N. Poulsen received the B.S. degree materials and metallurgical engineering from University of Arizona, Tucson, in 1984, the M.S. and Ph.D. degrees from the Department of Materials Science, University of Southern California, Los Angeles, in 1986 and 1988, respectively, and the M.Sc.E.E. from the Technical University of Denmark, Lyngby, Denmark, in 1995.

From 1995 to 2001, he worked first as a Research Associate and later as an Associate Research Professor in the field of high-speed wavelength-division multiplexing and optical time-division multiplexing. In 2001, he moved from Copenhagen, Denmark, to Santa Barbara, CA to join Calient Networks, where he worked on optical amplification and performance monitoring for all-optical microelectromechanical-based switches. He is currently working as an Associate Project Scientist in the Optical Communications and Photonics Network Group with Prof. D. J. Blumenthal with the Department of Electrical and Computer Engineering at the University of California, Santa Barbara. His main research area is all-optical packet switching using all-optical interferometric structures. His main interests were ultrahigh-speed optical-signal processing using nonlinear fiber and semiconductor material, mainly semiconductor optical amplifiers, interferometric structures, and electroabsorption modulators.

Steven P. DenBaars (M'91–SM'03–F'05) received the B.S. degree in materials and metallurgical engineering from the University of Arizona, Tucson, in 1984 and the M.S. and Ph.D. degrees from the University of Southern California, Los Angeles, in 1986 and 1988, respectively.

He was a member of the technical staff at Hewlett-Packard from 1988 to 1991, where he was involved in the fabrication of high-brightness light-emitting diodes. In 1991, he joined the faculty of the University of California, Santa Barbara (UCSB) where he is developing new solid-state optoelectronic devices. He is currently a Professor of materials and electrical engineering with the Materials Department, UCSB. Currently, he is an Associate Director of the Solid-State Lighting and Display Center at UCSB, which is developing new more energy-efficient light sources. His research also involves metal–organic chemical-vapor-deposition growth of GaN and InP-based tunable lasers and detectors. Special interests include the effect of materials' properties on device performance, blue VCSEL lasers, and microwave power transistors. He has authored over 200 technical publications, three book chapters, and 100 conference presentations, and is the holder of seven patents.

Prof. DenBaars received an NSF Young Scientist Award in 1995 and the Young Scientist Award from the International Symposium on Compound Semiconductors in 1998.

Larry A. Coldren (S'67–M'72–SM'77–F'82) received the Ph.D. degree in electrical engineering from Stanford University, Stanford, CA, in 1972.

After 13 years in the research area at Bell Laboratories, he joined the University of California, Santa Barbara, in 1984, where he currently holds appointments in materials and electrical and computer engineering, and is Director of the Optoelectronics Technology Center. In 1990, he cofounded Optical Concepts, later acquired as Gore Photonics, to develop novel vertical-cavity surface-emitting laser (VCSEL) technology. In 1998, he cofounded Agility Communications to develop widely tunable integrated transmitters. He is currently the Fred Kavli Professor of Optoelectronics and Sensors at the University of California, Santa Barbara. At Bell Laboratories, he initially worked on waveguided surface-acoustic-wave signal-processing devices and coupled-resonator filters. He later developed tunable coupled-cavity lasers using novel reactive-ion etching technology that he created for the then new InP-based materials. At the University of California, Santa Barbara, he continued work on multiple-section tunable lasers, inventing the widely tunable multielement-mirror concept in 1988. During the late 1980s, he also developed efficient vertical-cavity multiple-quantum-well modulators, which led to novel VCSEL designs that provided unparalleled levels of performance. He continues to be active in developing new photonic integrated circuit (PIC) and VCSEL technology, including the underlying materials growth and fabrication techniques. In recent years, for example, he has been involved in the creation of vertical and in-plane GaN-based emitters, efficient all-epitaxial InP-based VCSELs, and a variety of PICs incorporating numerous optical elements for widely tunable integrated transmitters, receivers, and wavelength converters. He has authored or coauthored over 700 papers, five book chapters, and one textbook, and has been issued 36 patents.

Prof. Coldren has presented dozens of invited and plenary talks at major conferences, he is a Fellow of Optical Society of America and of the Institute of Electrical Engineers, received the 2004 John Tyndall Award, and is a member of the National Academy of Engineering.